
Article:
Yang, H., Zhu, Z.Q. orcid.org/0000-0001-7175-3307, Lin, H. et al. (1 more author) (2018) Comparative study of hybrid PM memory machines having single- and dual-stator configurations. IEEE Transactions on Industrial Electronics, 65 (11). pp. 9168-9178. ISSN 0278-0046

https://doi.org/10.1109/TIE.2018.2823703

Comparative Study of Hybrid PM Memory Machines Having Single- and Dual-Stator Configurations

***Abstract*- In this paper, the memory flux principle is extended to switched flux structures, forming two newly emerged switched flux memory machines (SFMMs) with single-stator (SS) and dual-stator (DS) configurations. Two types of permanent magnets (PMs), i.e., NdFeB and low coercive force (LCF) PMs, are located in the stationary part. Thus, the developed machines can achieve easy online PM magnetization control, excellent air-gap flux control, and acceptable torque capability. In order to address the issue about the limited stator space encompassing dual PMs and magnetizing coils in the SS-SFMM, a DS design is further developed, where all excitations are placed on a separate inner stator to improve the torque density. A comparative study between the SFMMs with SS and DS structures is established. The investigated machine topologies and operating principle are described first based on a "U"-shaped hybrid PM arrangement, and the PM sizing of the DS machine is optimized with a simplified magnetic circuit model. In addition, the electromagnetic characteristics of the SFMMs with SS and DS structures are investigated and compared by finite-element (FE) method. The FE results are validated by the experiments on two fabricated prototypes.**

***Index Terms*—Dual stator, hybrid permanent magnet (PM), memory machine, partitioned stator, switched flux, variable flux.**

I. Introduction

VARIABLE-FLUX permanent-magnet (PM) machines [1]-[19] have been considered as an enabling solution to allow flexible air-gap flux adjustment and effective speed range extension. Meanwhile, the possibility of an inverter fault caused by excessively high back-EMF at high speed operation is attenuated. Therefore, VFPM machines were widely researched as a competent candidate for various applications requiring wide-speed-range operation [1]-[4]. In recent years, memory machines equipped with low-coercive-force (LCF) PMs have gained growing research interests [8]-[19]. For memory machines, the magnetization states of the LCF PM can be conveniently adjusted by applying a remagnetizing or demagnetizing current pulse. Consequently, the excitation copper loss is negligible during the flux regulation. Thus, high efficiency can be maintained within a wide operating range. Generally, memory machines can be divided into AC- and DC-magnetized types according to the winding types supplying the current pulse.

The concept of "memory machine" was firstly implemented in a sandwiched interior PM machine [9], where a temporary *d*-axis current pulse is applied in AC armature windings to vary the magnetization states of LCF PMs. Since then, various conventional interior PM machines [9]-[14] have been converted to memory machines. However, for DC-magnetized type, several machines having magnets on the stator (i.e., doubly salient [14] [15], variable reluctance [16], and switched flux (SF) [16]-[19] topologies) were extended to memory machines. Additional DC magnetizing coils are employed to generate a current pulse, facilitating the online magnetization control. Several advantages such as excellent rotor robustness and easy thermal dissipation can be obtained as well. Besides, two sets of magnets are used in order to improve the torque density, i.e. NdFeB and LCF PMs. In these cases, both excellent low speed high torque and high speed flux-weakening capability can be obtained.

Compared to those doubly salient [14] [15], variable reluctance [17] topologies, SF memory machines (SFMMs) [16]-[19] exhibit basically sinusoidal phase flux linkage, higher torque capability and lower torque ripple. Nevertheless, for those previously reported machines having a single-stator (SS) structure, the crowded stator results in the significant geometric conflict between magnets and windings. Meanwhile, the armature areas are accordingly reduced, leading to compromised torque density and high design difficulty. Very recently, the dual stator (DS) SFMMs [18] [19] were developed in order to deal with the above-mentioned issues. In the DS structure, the PMs sandwiched in stator teeth in the conventional SS design are moved to a secondary inner stator, and hence the armature areas are increased, which is helpful for the torque density improvement [20]. The armature windings and PM excitations are separately located on two stators, respectively. The inner stator permits sufficient space for encompassing dual PMs and magnetizing coils, and the geometric conflict between magnetic and electric loadings in the conventional SS one is alleviated [18]. Hence, high torque density and energy-efficient flux control capability can be simultaneously realized. However, the previous studies mainly focus on the machine topology development and performance analysis in individual cases. A quantitative comparison of SS- and DS-SFMMs is still unreported, and the specific benefits of the DS design for the performance improvement of the SFMM has not been identified and quantified. To fill this gap, a simplified analytical model is introduced to provide an in-depth understanding of the operating principle and the design tradeoff of this type of machines. The main contribution of this paper is to present a comprehensive comparative study of the SFMMs with SS and DS structures. The analytical modeling is employed to identify the key design challenges, as well as establish general design guidelines for the developed SFMMs with a general "U"-shaped dual PM arrangement. Then, the hybrid magnet sizing ratio is analytically optimized, which facilitates the further design parameter optimization. Finally, the key electromagnetic characteristics of the two types of SFMMs are comprehensively compared, and the experimental evaluation is presented as well.

This paper is organized as follows. In Section II, the investigated machine topologies are described based on a general "U"-shaped hybrid PM arrangement. Besides, the

operating principle, features and analysis methodology of the developed machines are introduced. In addition, in the Section III, the simplified magnetic circuits are modelled to unveil the underlying design tradeoff existing in the SFMMs. The hybrid magnet sizing is then optimized with the analytical method. Section IV is devoted to the performance evaluation and comparison of the SFMMs with SS and DS arrangements are presented in. The FE results are verified by experiments on two fabricated prototypes. In Section V.

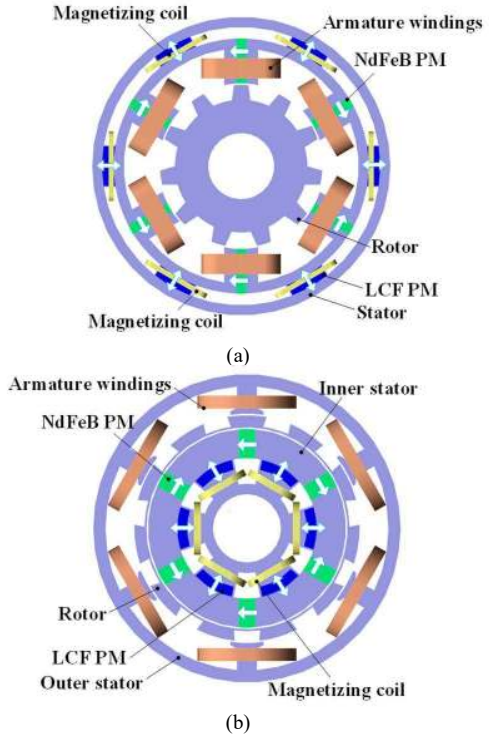

Fig. 1. The SFMM topologies. (a) Single stator. (b) Dual stator.

II. Configurations and Operating Principle of Single- and Dual-Stator SFMMs

A. Machine Configurations

Fig. 1 shows the SS- and DS-SFMM configurations, both characterized by a typical parallel magnetic circuit of the tangentially magnetized NdFeB PMs and the radially magnetized LCF PMs sandwiched between the outer stator ring and the inner stator pole. The corresponding simplified "U"-shaped hybrid PM arrangements [13] for the two machines are illustrated in Fig. 2. The SS structure can be considered as a conventional switched flux permanent magnet (SFPM) machine [21] plus an additional stator ring and LCF PMs embedded between the stator yoke and the "U"-shaped stator segments. Different from the SS counterpart, the DS-SFMM is characterized by the separate PM and armature excitations on the outer and inner stators, respectively. The rotor pole pieces are sandwiched between the two stators, which are geometrically similar to magnetically geared machines [22] [23]. The outer stator with non-overlapping armature windings resembles the conventional tooth-coil PM machine. The radially magnetized LCF PMs behave as flux adjustors, and the spoke-type NdFeB PMs allow the flux-concentrating effect to increase the torque density. Evidently, for the single stator structure as illustrated in Fig. 1(a), the significant geometric conflicts can be observed on the stator due to the existence of two sets of windings and hybrid magnets within one stator. If the armature winding is removed as shown in Fig. 1(b) in the DS structure, the geometric conflicts between the PMs and armature windings can be alleviated.

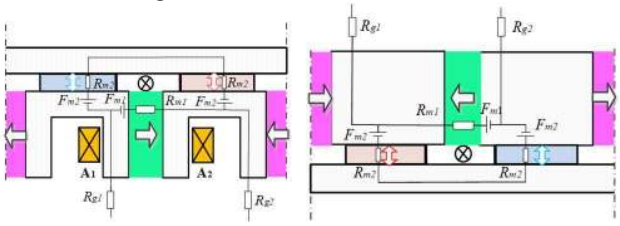

Fig. 2. General "U"-shaped hybrid PM arrangement for SFMMs. (a) Single stator. (b) Dual stator.

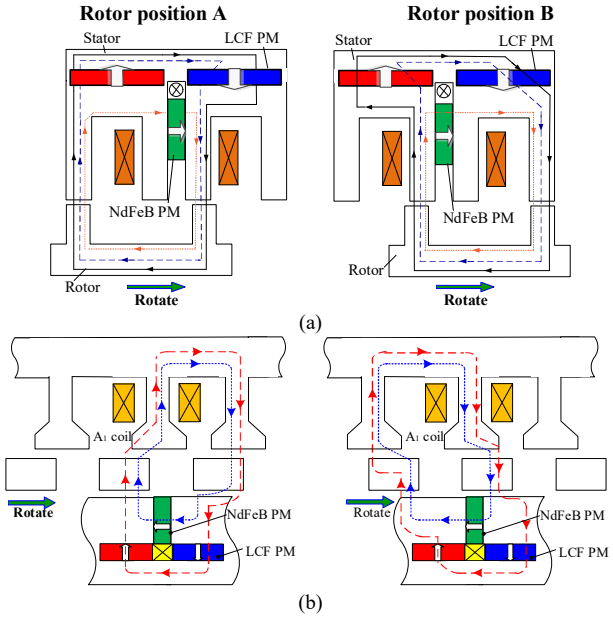

Fig. 3. The operating principle of SFMMs. (a) Single stator. (b) Dual stator.

B. Operating Principles

The operating principles of the SFMMs are illustrated in Fig. 3. Firstly, the operating principle of the DS-SFMM is essentially similar to that of the SS-SFMM, the PM pole number is identical to that of the outer stator teeth, which allows switched flux action via alignment/misalignment between rotor segments and two separate stator parts. Secondly, the machine consists of two stationary excitations and sandwiched rotor segments, which is similar to a magnetically geared machine [23], i.e., the abundant harmonics arising from the modulation of rotor segments contribute to torque production [23].

On the other hand, the developed machines can be considered as the application of the memorable flux concept to the SF structure. The flux-adjusting principle can be illustrated by a simplified hysteresis model of LCF PMs, namely, nonlinearity-involved parallelogram hysteresis model (NIPHM) [16], as shown in Fig. 4. In this model, the major hysteresis loops and all the minor loops are assumed to have identical value of coercive force H_c, but different values of remanence B_{rk}. The set of recoil lines labeled with l_1 can be expressed as:

$$B = \mu_0 \mu_r H_m + B_{r1k}, \quad n = 1,2,3\ldots. \tag{1}$$

where μ_0 and μ_r are the vacuum permeability and the relative permeability of LCF PM respectively; H_m is the positive magnetic field intensity, and B_{r1k} represents the corresponding k^{th} remanence of the sets of hysteresis loops.

A magnetization ratio k_{mr} can be defined as the ratio of B_{r1k} to the remanence B_{r1}, i.e.

$$k_{mr} = B_{r1k} / B_{r1}, \quad k = 1,2,3\ldots. \tag{2}$$

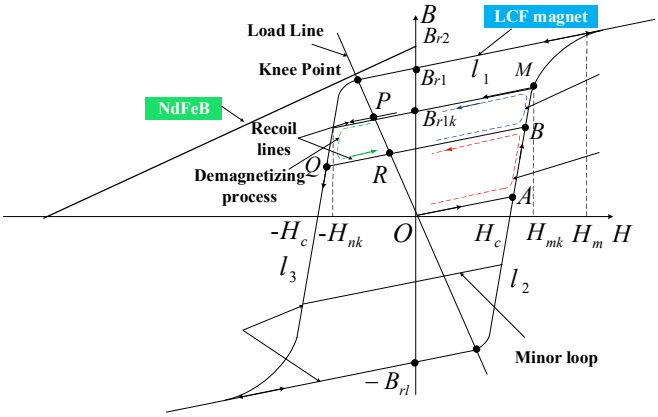

Fig. 4. Illustration of the simplified hysteresis model (NIPHM) of LCF PM.

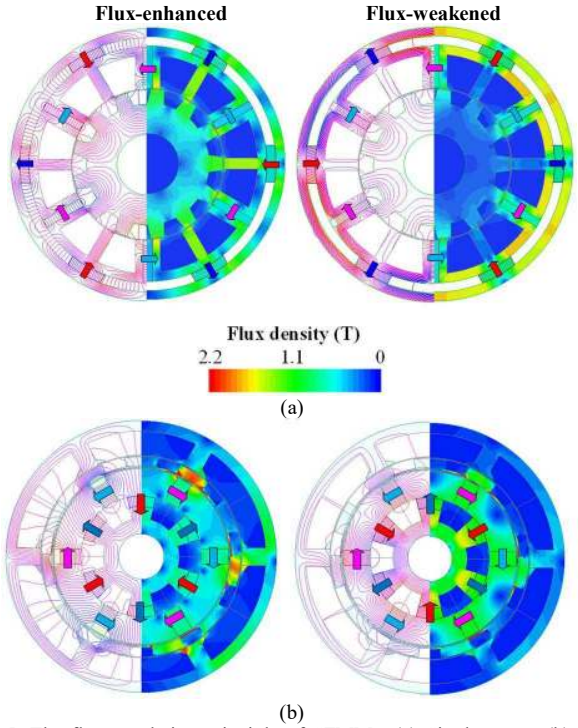

Fig. 5. The flux regulation principle of SFMMs. (a) Single stator. (b) Dual stator.

Evidently, k_{mr} ranges from -1 and 1, and the flux linkage can be flexibly changed as the operating points of LCF PMs shift along the different recoil lines. Typically, the "flux-enhanced" and "flux-weakened" states refer to k_{mr} of "1" and "-1", which indicate that the LCF PMs are magnetized identically and oppositely with NdFeB PMs, respectively. Furthermore, "zero magnetization" state corresponds to k_{mr}="0". Fig. 5 shows the corresponding open-circuit field distributions of the SFMMs under the flux-enhanced and flux-weakened states, respectively. With the aid of the online magnetization, the NdFeB magnetic fields are enforced to air-gap or magnetically short-circuited by LCF PMs, and hence the air-gap flux density can be accordingly enhanced or weakened.

C. Finite Element Analysis Considering Hysteresis Modeling

In order to simplify the computational effort and consider the nonlinear hysteresis behavior of LCF PMs, a NIPHM for LCF PM [16] is utilized and coupled with FE method. In this case, The FE software package-JMAG 15.1 is employed, and the NIPHM for LCF PMs is compiled in "user subroutine module" to simulate the hysteresis behavior. The flowchart of the coupling solution with particular emphasis on the magnetization initialization and adjustment is shown in Fig. 6.

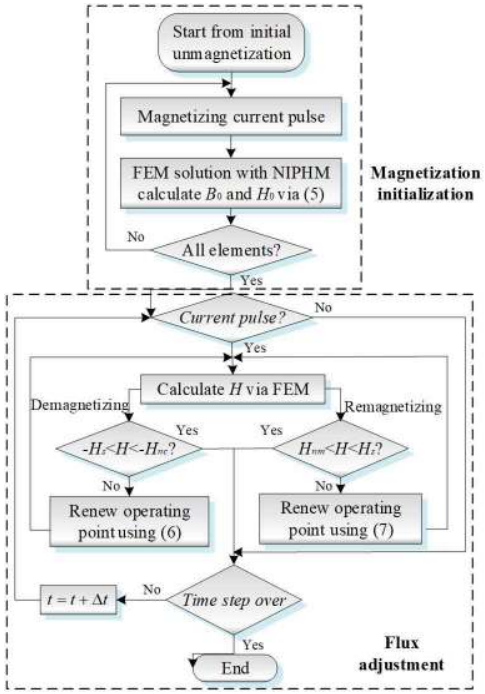

Fig. 6. Flowchart of the coupling solution.

The two lines of the major loops and the minor loops can be generally approximated by two polynomial functions by taking the saturated magnetization into account, where l_2 and l_3 can be respectively expressed as:

$$H = f(B) = A_0 + A_1 B + A_2 B^2 + A_3 B^3. \tag{3}$$

$$H = -f(-B) = -A_0 + A_1 B - A_2 B^2 + A_3 B^3. \tag{4}$$

where the coefficients A_0, A_1, A_2, and A_3 can be determined by statistical fitting using experimental data. As shown in Fig. 4, the operating point of LCF PM can be determined by the intersection of load line and recoil line, and the operating point will shift along different recoil lines based on the applied remagnetizing or demagnetizing MMFs.

During the magnetization initialization, all the remanences of PM elements are set to be zero first. When applying a temporary flux intensity H_0, the operating point will move along *OAMP* and stabilizes at point *P*, and the corresponding remanence B_{rP} can be derived as:

$$B_{rP}=\begin{cases}0, & 0\le H_0\le H_c\\ f^{-1}(H_0)-\mu_r\mu_0 H_0, & H_c\le H_0\le H_m\\ B_{r1}, & H_m\le H_0\end{cases} \quad (5)$$

During the demagnetizing status, the operating point will track along *PQR* and finally arrive at point *R* with the corresponding remanence B_{rR} deduced as:

$$B_{rR}=\begin{cases}B_{rk} & -H_{nk}\le H\le 0\\ -f^{-1}(-H)-\mu_r\mu_0 H, & -H_m\le H\le -H_{nk}\\ -B_{r1} & H\le -H_m\end{cases} \quad (6)$$

If a remagnetizing flux intensity *H* is applied, the operating point will shift along *RBMP* and return to point *P* with the relevant remanence B_{rS} deduced as:

$$B_{rS}=\begin{cases}B_{rk}, & 0\le H\le H_{mk}\\ f^{-1}(H)-\mu_r\mu_0 H, & H_{mk}\le H\le H_m.\\ B_{r1}, & H_m\le H\end{cases} \quad (7)$$

III. Design Considerations

A. Analytical Modeling

The design considerations of the SFMMs can be analyzed based on the simplified magnetic circuits as illustrated in Fig. 2, where the dual PMs are magnetically in parallel. Thus, the air-gap fluxes corresponding to flux-enhanced ($\Phi_{\delta+}$) and flux-weakened ($\Phi_{\delta-}$) states can be simplified and formulated as

$$\Phi_{\delta+}=\frac{H_{c2}\mu_0\mu_{r2}A_{m2}+H_{c1}\mu_0\mu_{r1}A_{m1}}{R_g\left(\frac{\mu_0\mu_{r1}}{h_{m1}}A_{m1}+\frac{\mu_0\mu_{r2}}{2h_{m2}}A_{m2}\right)+1} \quad (8)$$

$$\Phi_{\delta-}=\frac{H_{c2}\mu_0\mu_{r2}A_{m2}-H_{c1}\mu_0\mu_{r1}A_{m1}}{R_g\left(\frac{\mu_0\mu_{r1}}{h_{m1}}A_{m1}+\frac{\mu_0\mu_{r2}}{2h_{m2}}A_{m2}\right)+1} \quad (9)$$

where H_{c1} and H_{c2} are the coercive forces of LCF and NdFeB PMs, respectively; h_{m1} and h_{m2} are the thicknesses of LCF and NdFeB PMs, respectively; A_{m1} and A_{m2} denote the cross-sectional areas of LCF and NdFeB PMs, respectively; μ_{r1} and μ_{r2} are the relative permeabilities of LCF and NdFeB PMs, respectively; μ_o is the vacuum permeability, and R_g is the air-gap magnetic reluctance. The flux adjusting ratio α_{mag} is defined as the ratio of $\Phi_{\delta+}$ to $\Phi_{\delta-}$ for indicating the maximal achievable variable speed range.

$$\alpha_{mag}=\frac{H_{c2}\mu_{r2}A_{m2}+H_{c1}\mu_{r1}A_{m1}}{H_{c2}\mu_{r2}A_{m2}-H_{c1}\mu_{r1}A_{m1}}=\frac{\frac{H_{c2}\mu_{r2}A_{m2}}{H_{c1}\mu_{r1}A_{m1}}+1}{\frac{H_{c2}\mu_{r2}A_{m2}}{H_{c1}\mu_{r1}A_{m1}}-1} \quad (10)$$

It can be deduced that the flux adjusting range increases with the ratio of H_{c2} to H_{c1}. In order to establish the relationship between the cross-sectional ratio of PMs and maximal air-gap flux, (8) can be rewritten as

$$\Phi_{\delta+}\approx\frac{2H_{c2}h_{m2}}{R_g}+\left(\frac{\mu_{r2}(H_{c1}h_{m1}-2H_{c2}h_{m2})}{R_g\left(\frac{\mu_0\mu_{r1}}{2}\frac{h_{m2}}{h_{m1}}\frac{A_{m2}}{A_{m1}}+\mu_0\mu_{r2}\right)}\right) \quad (11)$$

It can be concluded that the NdFeB PM dominates the torque production, and the second term in (11) is less than zero due to "$H_{c1}h_{m1}<2H_{c2}h_{m2}$" in this case. Thus, the design tradeoff exists in this type of machine from (10) and (11) since increasing the magnet cross-sectional ratio enhances the torque density, while decreases the flux-adjusting capability [18].

It should be noted that in the DS-SFMM, there is no significant conflict between magnet parameters and slot areas existing in the SS counterpart, and hence facilitate the magnet sizing to satisfy the desired performance requirement.

B. Hybrid Magnet Sizing Refinement

With the aid of the magnetic circuit method as detailed in the preceding section, the magnet sizing is preliminarily optimized as a predominant parameter. The variations of normalized maximum air-gap flux and flux adjusting ratio with the magnet cross-sectional ratio (A_{m2}/A_{m1}) of the DS-SFMM are computed and compared with FE predictions in Fig. 7. It can be observed that the analytical predictions agree well with those obtained by the FE method. Therefore, the optimal cross-sectional ratio can be obtained, i.e. ~1.5, which properly balances the torque and flux adjusting capabilities.

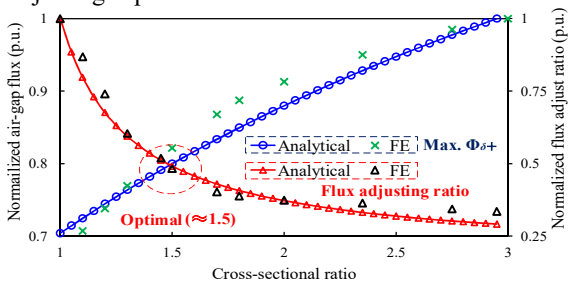

Fig. 7. Analytical- and FE-predicted variations of normalized maximum air-gap flux and flux adjusting ratio with the magnet cross-sectional ratio.

With the optimized ratio of dual magnet cross-sectional areas, the magnet thickness ratio can be optimized. It is worth emphasizing that the locations of the operating points of the LCF PM should be considered first. Therefore it is essential to stabilize the operating points on the upper recoil line at the flux-enhanced state, i.e. linear operating region, which enables the LCF PM to avoid the pre-demagnetization before flux control. The fluxes generated by the LCF and NdFeB PM branches at flux-enhanced states can be respectively governed by

$$\Phi_{\delta 1+}=\frac{\frac{H_{c2}h_{m1}h_{m2}}{\mu_0\mu_{r1}A_{m1}}+\left(\frac{1}{2}H_{c2}h_{m2}-H_{c1}h_{m1}\right)\cdot R_g}{R_g\left(\frac{h_{m2}}{\mu_0\mu_{r2}A_{m2}}+\frac{2h_{m1}}{\mu_0\mu_{r1}A_{m1}}\right)+4\frac{h_{m2}}{\mu_0\mu_{r2}A_{m2}}\frac{h_{m1}}{\mu_0\mu_{r1}A_{m1}}} \quad (11)$$

$$\Phi_{\delta 2+}=\frac{\frac{H_{c1}h_{m1}h_{m2}}{\mu_0\mu_{r2}A_{m2}}+\left(H_{c1}h_{m1}-\frac{1}{2}H_{c2}h_{m2}\right)\cdot R_g}{R_g\left(\frac{h_{m2}}{\mu_0\mu_{r2}A_{m2}}+\frac{2h_{m1}}{\mu_0\mu_{r1}A_{m1}}\right)+4\frac{h_{m2}}{\mu_0\mu_{r2}A_{m2}}\frac{h_{m1}}{\mu_0\mu_{r1}A_{m1}}} \quad (12)$$

As a result, the variations of normalized individual branch fluxes contributed by dual magnets are analytically calculated and compared with FE-predicted results in Fig. 8. Evidently, the NdFeB flux increases with the ratio of NdFeB to LCF magnet thickness, while the tendency reverses for LCF PM flux. This is due to the fact that the NdFeB PM dominates the major air-gap flux. Meanwhile, the optimal magnet thickness ratio (h_{m2}/h_{m1}) approximates to 0.75, which well balances the two individual branch contributions. Furthermore, it can be found

that the pre-demagnetization of LCF PMs can be effectively prevented via the optimal design. With the aid of analytical method, the hybrid magnet sizing is firstly optimized as a predominant parameter. Then, other design parameters will be globally optimized to maximize the average torque with the constraints of the optimal dual magnet sizing ratio and copper loss of 30W.

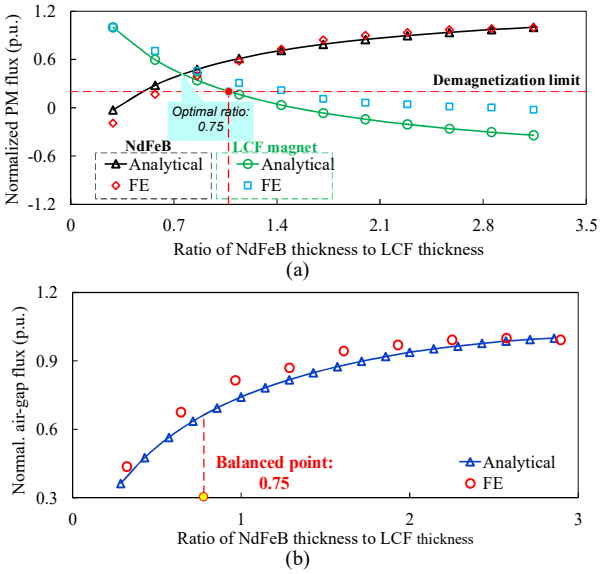

Fig. 8. Analytical- and FE-predicted variations of normalized branch fluxes and air-gap flux (flux-enhanced state) with the magnet cross-sectional ratio. (a) Magnet branch fluxes. (b) Resultant air-gap flux.

TABLE I
KEY DESIGN PARAMETERS OF THE SF- AND DS-SFMMS

Machine types	Dual stator	Single stator
Rated speed (r/min)	400	
Rated current density (A/mm^2)	6.5	
Rated current (Arms)	15	
Outer diameter of outer stator (mm)	90	
Inner diameter of outer stator (mm)	62	56
Outer stator tooth arc (deg.)	11	12
Outer stator tooth-tip width (mm)	6.5	
Outer diameter of inner stator (mm)	56	n/a
Outer air-gap length (mm)	0.5	0.5
Inner air-gap length (mm)	0.5	n/a
Arc of outer/inner rotor (deg.)	14/16	18
Rotor segment thickness (mm)	5	n/a
Active stack length (mm)	25	
LCF PM thickness×length (mm)	3/12	5.14/7
NdFeB PM thickness×length (mm)	2.76/15	4.60/9
PM volume (cm^3)	116.10	
Magnet mass (kg)	0.082	
Outer stator mass (kg)	1.70	2.06
Rotor mass (kg)	1.20	1.36
Inner stator mass (kg)	1.10	-
NdFeB PM grade	N35SH	
NdFeB PM remanence	1.2T	
LCF PM grade	SB12B	
LCF PM remanence	0.8T	
Number of armature turns per coil	84	
Number of magnetizing turns per coil	100	
Fill factor	0.5	
Steel grade	35CS300	

C. Feasible Stator Slot/Rotor Pole Number Combination

For obtaining the symmetric back-EMF waveforms, the combination of the stator slot/rotor pole number N_s/Z_r in the SFMMs must comply with

$$N_r / GCD(Z_r \,\&\, N_s) = 2N_{ph}i \quad i=1,2,3,4... \tag{13}$$

where GCD denotes the greatest common divisor, N_{ph} is the number of the phase. The distribution factor k_d and pitch factor k_p can be computed based on the principle of SF machines [21],

$$k_d = \sin(Qk\alpha/2) / \left[Q\sin(k\alpha/2)\right] \tag{14}$$

$$k_p = \cos\left[\pi k\left(Z_r/N_s - 1\right)\right] \tag{15}$$

where Q is the number of the least EMF vectors per phase, α is the angle between two adjacent vectors, and k is the harmonic order. Thus, for the 6-stator slot cases, the feasible rotor pole number is close to the multiples of stator pole number. In this paper, the 6/11 stator slot/rotor pole combination is selected based on the parametric study in [17] [18]. The design parameters of the two investigated machines are listed in Table I. It should be noted that the two machines share identical overall dimensions, the armature/magnetizing winding turns, magnet usage and rated copper loss for fair comparison.

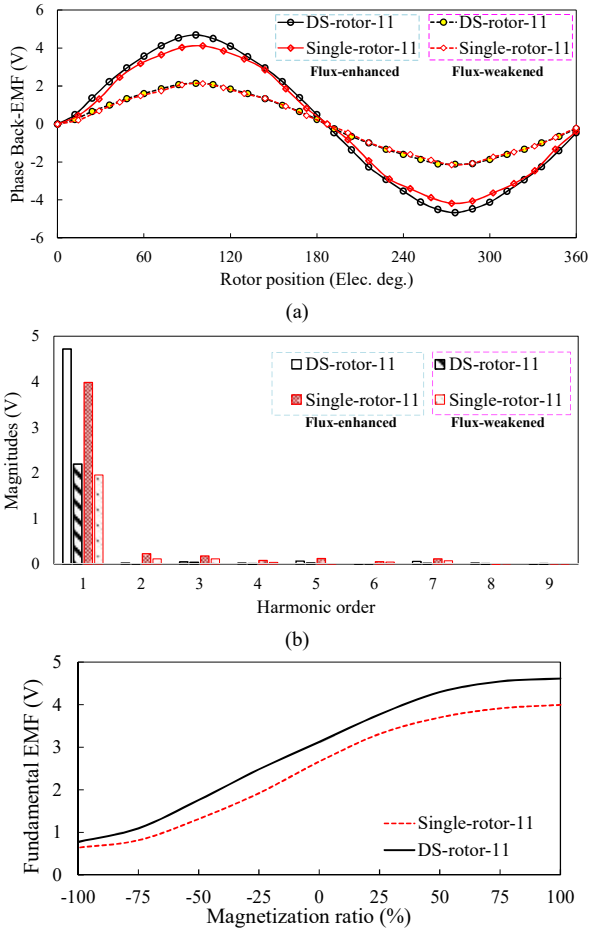

Fig. 9. Back-EMF waveforms. (a) Waveforms. (b) Harmonic spectra. (c) Variation of back-EMF fundamental magnitude with the magnetization ratio of LCF PMs.

IV. ELECTROMAGNETIC PERFORMANCE COMPARISON

A. Flux Regulation Capability

The open-circuit back-EMFs and harmonic spectra of the two machines under different magnetization states are shown in Figs. 9(a) and (b), respectively. Obviously, the DS machine exhibits the higher EMF magnitude at the flux-enhanced state. Moreover, the fundamental back-EMFs as functions of the magnetization ratio of LCF PMs are plotted in Fig. 9(c). It can

be observed that the DS machine shows slightly wider flux regulation range due to greater magnetic saturation in the stator of the SS structure caused by the crowded stator structure.

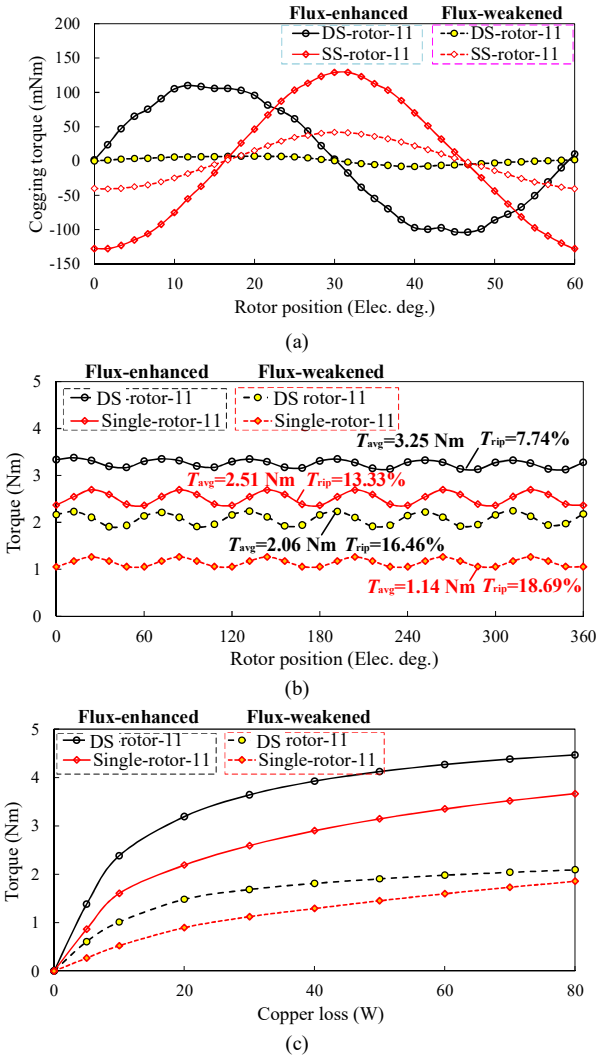

Fig. 10. Torque characteristics. (a) Cogging torque. (b) Steady-state torque, I_d=0, copper loss=30W. (c) Torque versus copper loss characteristics, I_d=0.

B. Torque Characteristics

The cogging torque and on-load torque waveforms under different magnetization states are shown in Fig. 10. From Figs. 10(a) and (b), the slightly higher cogging torque and torque ripple can be observed in the SS machine regardless of the magnetization state. This is mainly resulted from the larger 5th and 7th order harmonics in the back-EMFs of SS-SFMM, as reflected in Fig. 9(b). The torque against copper loss characteristics of the two machines are compared as shown in Fig. 10(c). It demonstrates that with the identical copper losses, the proposed DS-SFMM can deliver 29.5% higher torque than its SS counterpart at flux-enhanced state.

C. Demagnetization Withstand Capability

The cross-coupling demagnetization withstand capability of the proposed DS machine should be further examined. The cross-coupling demagnetization ratio (DR) can be defined as

$$DR = \left(E_1 - E_2\right) / E_1 \times 100\% \quad (16)$$

where E_1 and E_2 represent the fundamental back-electromotive forces (EMF) before and after applying q-axis current (40A).

The demagnetization behaviors of LCFs can be reflected by the open-circuit field distributions or the open-circuit working points of LCF PMs before and after applying an electrical period of q-axis current (40A) as shown in Fig. 11. The LCF PMs in the SS machine have experienced more significant cross-coupling demagnetization than its DS counterpart. Moreover, the variations of DR (%) of both DS and SS machines with the magnitude of the applied q-axis current are shown in Fig. 12. Overall, the working point of LCF PM in the SS machine is lower, and more susceptible to the on-load armature reaction. Thus, it indicates that the less iron magnetic saturation around PMs in the DS machine facilitates the stabilization of the working points of the LCF PMs, i.e., the higher demagnetization withstand capability.

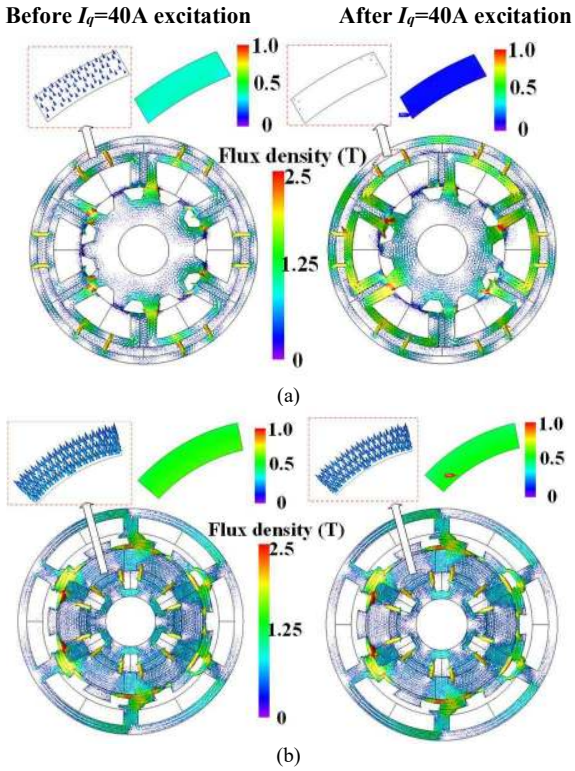

Fig. 11. Open-circuit field distributions before and after applying an electrical period of q-axis current=40A. (a) Single-stator machine. (b) Dual-stator machine.

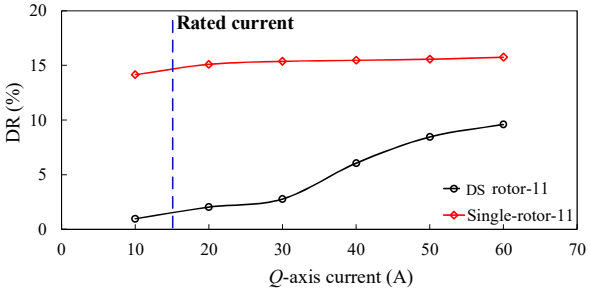

Fig. 12. Comparison of demagnetization ratios under various q-axis currents.

D. Flux-Weakening Performance

As a critical characteristic for SFMMs, the flux-weakening performance is evaluated. A flux-weakening factor k_{fw} that

indicates the capability extending the speed range above the base speed can be defined as

$$k_{fw} = \frac{L_d i_{\lim}}{N_a \Phi_\delta} \tag{17}$$

where i_{lim}, L_d, Φ_δ and N_a are the maximum phase current, d-axis inductance, PM flux linkage and the number of phase armature winding turns; As a result, the base speed ω_{base}, maximum speed ω_{max} and k_{fw} at different magnetization states are listed in Table II. It can be seen that the DS machine has higher flux-weakening capability than the SS counterpart for the given inverter power rating regardless of magnetization states.

TABLE II
COMPARISON OF FLUX-WEAKENING CHARACTERISTICS IN SS- AND DS-SFMMS, U_{LIM}=18.5V, I_{LIM}=15A

Machine types	State	Base speed (r/min)	Max. speed (r/min)	L_d (mH)	k_{fw}
Dual-stator	Enhan.	400	9300	0.76	0.93
	Zero	650	∞	0.86	1.17
	Weak.	950	∞	0.89	1.74
Single-stator	Enhan.	420	7250	0.79	0.79
	Zero	520	9600	0.82	0.95
	Weak.	720	∞	0.57	1.40

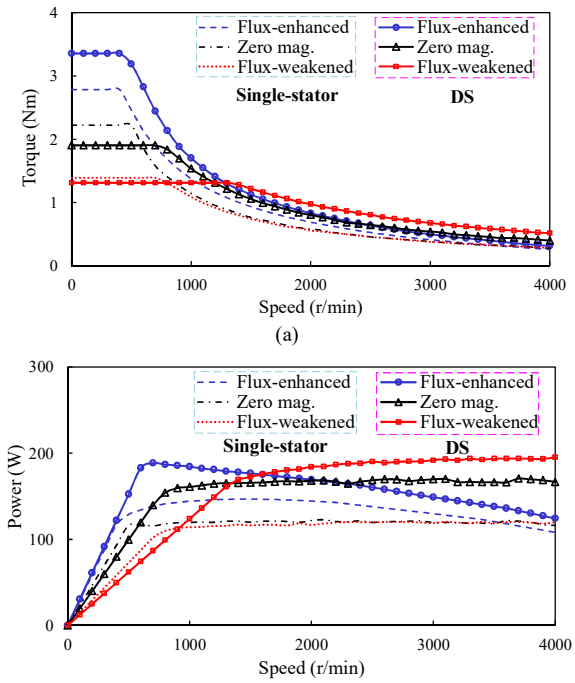

Fig. 13. FE-predicted torque-speed curves of the DS- and SS-SFMMs. (a) Torque-speed. (b) Power-speed.

The torque-speed curves are calculated by accounting for the cross-coupling saturation [26] [27]. The cross-coupling level in the torque-speed curve calculation depends on the estimation method of d/q-axis inductances and PM flux linkage. Based on the predetermined flux linkage versus dq-axis current data table, the torque-speed curves at different magnetization states are obtained as shown in Fig. 13. It can be observed that the proposed DS design can effectively extend the constant-power speed range due to the increased base speed and higher d-axis inductance at the flux-weakened state.

E. Evaluation of Iron Loss and Efficiency Maps

In order to illustrate the merits of the efficiency improvement over a wide operating range in SFMMs, the iron loss and efficiency characteristics of the 6-stator slot/11-rotor pole SFMMs are investigated. The rated-load iron loss distributions of the SS- and DS-SFMMs are shown in Fig. 14. Basically, the iron losses are obviously reduced in the two cases with the reduction of the magnetization level of LCF PMs. It can be observed that the highest iron loss density can be observed in the rotor poles of the two machines. Besides, the iron loss of the inner stator in the DS machine scarcely varies with the magnetization level change. Moreover, the iron losses in different components of the machines are listed in Table III. Overall, for the two investigated machines, the iron losses in both stator and rotor parts show a decreasing trend with the reduction of the PM flux linkage. Besides, due to the existence of an additional inner stator, the DS-SFMM exhibits higher iron loss than its SS counterpart regardless of the magnetization state.

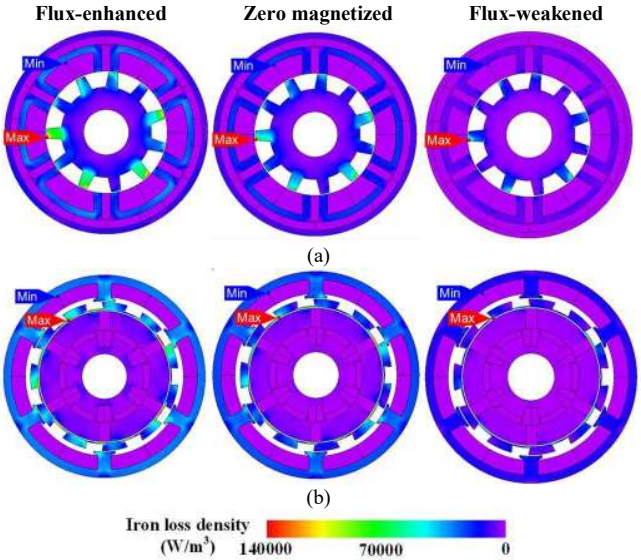

Fig. 14. The iron loss density distributions of the proposed 6-slot/11-rotor pole SS- and DS-SFMMs under rated load, I_d=0, copper loss=30W. (a) Single stator. (b) Dual stator.

TABLE III
COMPARISON OF IRON LOSS CHARACTERISTICS IN SS- AND DS-SFMMS, COPPER LOSS=30W.

Types	State	Outer stator	Rotor	Inner stator	Total
Dual-stator	Enhanced	1.19	0.38	0.18	1.75
	Zero	1.03	0.38	0.19	1.60
	Weakened	0.45	0.21	0.22	0.88
Single-stator	Enhanced	0.63	0.81	n/a	1.44
	Zero	0.50	0.74	n/a	1.24
	Weakened	0.22	0.39	n/a	0.61

By way of example, the iron loss and efficiency maps of the DS-SFMM are shown in Figs. 15 and 16, respectively. Overall, it can be observed that the iron loss is decreased due to the reduction of the PM flux linkage at the flux-weakened state. This will benefit the efficiency improvement in the high-speed flux weakening region, as evidenced in Fig. 16. In addition, it is obvious that the highest efficiency region locates at different speed regions for different magnetization states. Hence, it is practical to realize efficiency improvement within a wide operating envelop by combining the highest efficiency characteristics at different magnetization states. For example,

the flux-enhanced operation is preferred for constant-torque operation to obtain high efficiency, whereas the flux-weakened state is favorite to the constant-power operation with the minimized iron losses, which are the dominant loss component at high-speed region.

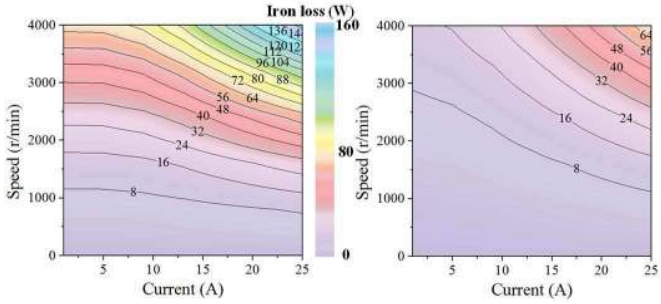

Fig. 15. FE-predicted iron loss maps of the proposed 6-slot/11-rotor pole DS-SFMM. (a) Flux-enhanced. (b) Flux-weakened.

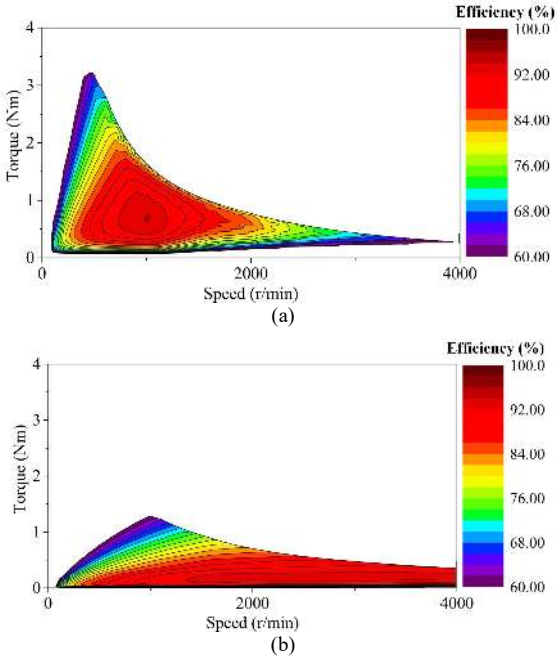

Fig. 16. FE-predicted efficiency maps of the proposed 6-slot/11-rotor pole DS-SFMM. (a) Flux-enhanced. (b) Flux-weakened.

V. Experimental Verification

In order to validate the preceding analyses, two prototypes having SS and DS configurations were manufactured and tested. The machine prototypes and test rig are shown in Fig. 17. The test platform for measuring the machine on-load performance is shown in Fig. 17(e). OSOKKI TS-7700 Torque Station is utilized to generate a load torque for the tested prototypes. Meanwhile, an encoder is used for rotor position detection and a torque transducer embedded in TS-7700 Torque Station is employed for torque measurement. Compared to the SS machine, since the manufacturing of the prototype is relatively mechanically complicated, the mechanical aspect should be considered [27]. As the rotor is a cantilever structure, the rotor iron pieces are encapsulated in epoxy resin, as shown in Fig. 16(c). The iron rib is employed to connect the individual rotor iron pieces, which can ease the fabrication. Then, the rotor pieces are encapsulated by resin and supported by the non-magnetic bars. The metallic sticks are embedded in the epoxy resin, and are linked with the end caps for fixation. Accordingly, the assembled rotor can be connected to the machine frame via bearings. It should be noted that the epoxy resin can provide certain mechanical strength since the tensile strength is 85N/mm². Hence, the DS prototype is able to tolerate certain severe working conditions. It is therefore essential to take some measures to cope with those working conditions, such as high speed or high torque application. For the high power-rating cases, another similar alternate solution such as the aluminum alloy reinforcement or carbon-fiber bandage can be employed.

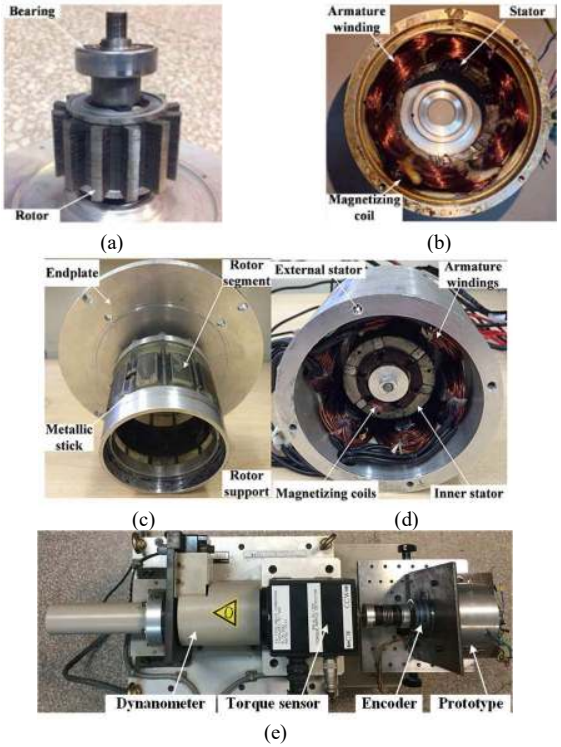

Fig. 17. The manufactured prototypes of the SFMMs: (a) Rotor (SS). (b) Stator (SS). (c) Rotor assembly (DS). (d) Stator (DS). (e) Test rig.

The phase back-EMFs for the two machines under various magnetization states have been measured and compared with FE-predicted ones in Fig. 18. Furthermore, the FE-calculated and tested torques versus q-axis current characteristics are shown in Fig. 19, respectively. Overall, it can be observed that the DS-SFMM can provide higher torque capability albeit of the magnetization states than its SS counterpart, while comparable flux regulation range can be observed in the two machines. In addition, relatively larger differences between FE and measured torque results can be observed in the low current cases. This is mainly resulted from the viscous friction and manufacture tolerance existing in the test rig, and hence the instantaneous torque under light-load operation is too small to be accurately measured by the torque meter. Furthermore, it shows that the 2D FE analyses significantly overestimate the back-EMF and torque results, while the 3D FE predictions agree well with the measurements. This is mainly attributed to the fact that end-effects and mechanical tolerance are not included in the 2D FE analyses. The 3D FE simulation is performed to clearly illustrate the end-effect, which is

represented by the outer air-gap flux density distribution along the axial direction of the DS-SFMM at no-load state as shown in Fig. 20. It can be seen that the end-effects lead to the reduction of the peak flux density in the active region by ~13.6%, as well as the end flux density reduction by ~61.7%.

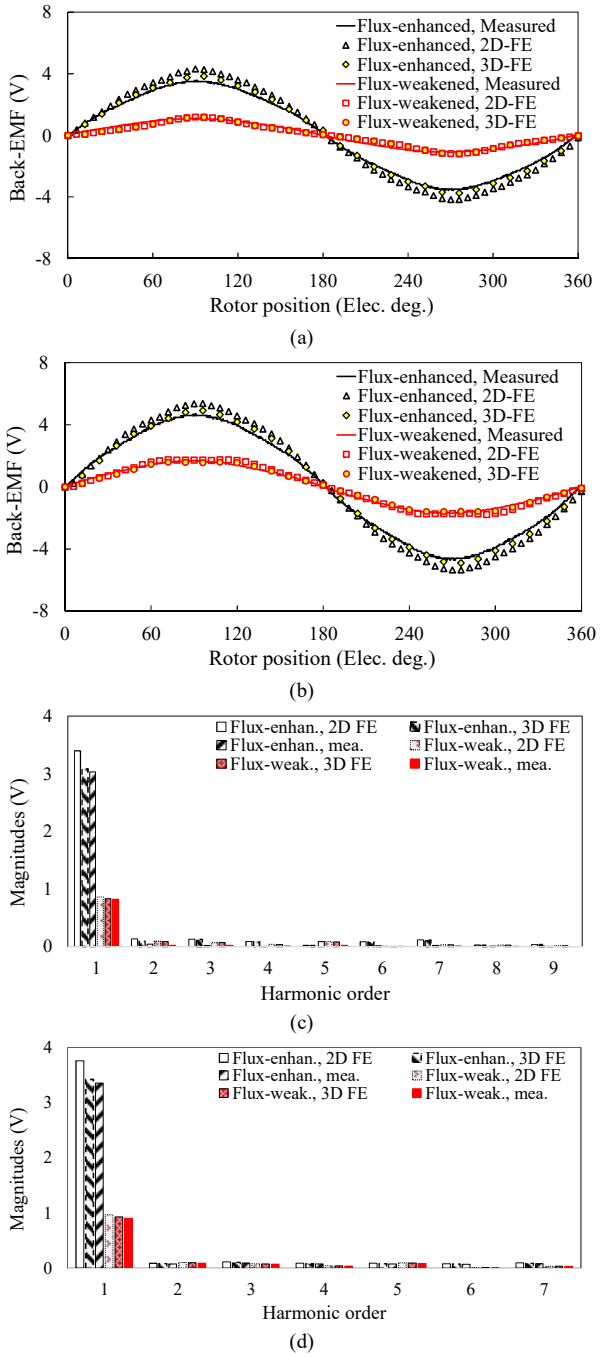

Fig. 18. Comparison of FE-predicted and measured phase back-EMF waveforms of the proposed DS-SFMMs. (a) Waveforms (SS). (b) Waveforms (DS). (c) Harmonic spectra (SS). (d) Harmonic spectra (DS).

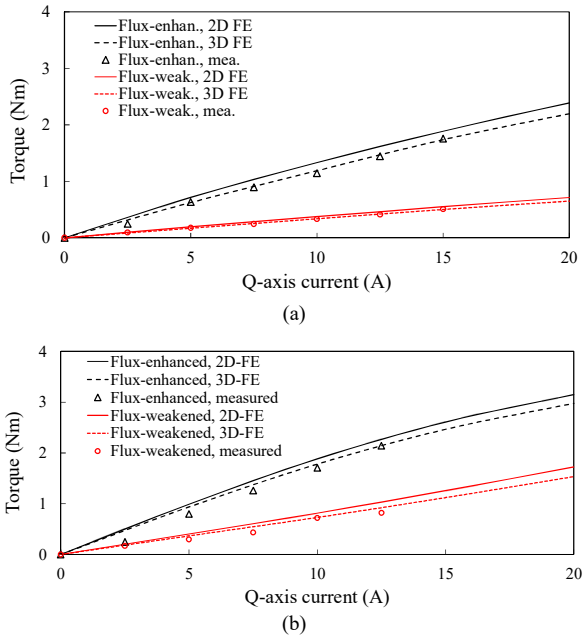

Fig. 19. Comparison of FE-predicted and measured torque against current characteristics of the SFMMs. (a) Single stator. (b) Dual stator.

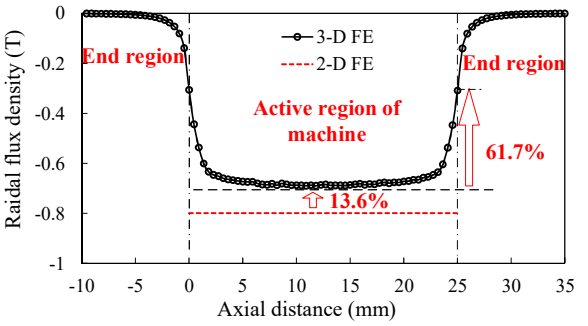

Fig. 20. The 3D/2D FE-predicted outer air-gap radial flux density distributions along the axial direction in DS-SFMM (open-circuit).

VI. Conclusions

In this paper, two SFMMs having SS and DS configurations are developed and compared. The DS design concept is applied to the SF structure in order to separate the magnetic and electric loadings, which allows the alleviation of geometric trade-off existing in the S-SFMM. The hybrid PM sizing of the DS machine is analytically optimized with the aid of a simplified magnetic circuit model. Based on the electromagnetic performance comparison, the DS machine exhibits higher torque density than its SS one. In addition, the DS-SFMM exhibits better demagnetization withstand capability than the SS one since the LCF magnets in the DS one are less exposed to the severe magnetic saturation on the stator. Besides, the proposed DS machine has better capability to extend the speed range for the given inverter power rating, regardless of magnetization states, and the efficiency improvement can be achieved within a wide operating envelop. Finally, two prototypes having SS and DS configurations respectively are fabricated and tested, which confirms that the DS-SFMM can achieve higher torque capability than its SS counterpart. Meanwhile, it can be found that the two machine can offer effective and efficient flux control. Nonetheless, the DS-SFMM

still suffers from two relatively more complicated structure and manufacturing cost than the SS machine. With the development of dual mechanical port machines and material technology, the mechanical issues, particularly under extreme conditions, will be better managed in the future.

VII. References

[1] Z. Q. Zhu and D. Howe, "Electrical machines and drives for electric, hybrid, and fuel cell vehicles," *Proc. IEEE*, vol. 95, no. 4, pp. 746-765, Apr.2007.

[2] A. El-Refaie, "Fractional-slot concentrated-windings synchronous permanent magnet machines: opportunities and challenges," *IEEE Trans. Ind. Electron.*, vol. 57, no. 1, pp. 107-121, Jan. 2010.

[3] M. Cheng, W. Hua, J. Zhang, W. Zhang, "Overview of stator-permanent magnet brushless machines," *IEEE Trans. Ind. Electron.*, vol. 58, no. 11, pp. 5087-5101, Nov. 2011.

[4] W. L. Soong and T. J. E. Miller, "Field-weakening performance of brushless synchronous AC motor drives," *IEE Proc. Electr. Power Appl.*, vol. 141, no. 6, pp. 331-340, Nov. 1994.

[5] Z. Zhang, Y. Tao, and Y. Yan, "Investigation of a new topology of hybrid excitation doubly salient brushless DC generator," *IEEE Trans. Ind. Electron.*, vol. 59, no. 6, pp. 2550–2556, Jun. 2012.

[6] Y. Wang, Z. Deng, and X. Wang, "A parallel hybrid excitation flux-switching generator DC power system based on direct torque linear control," *IEEE Trans. Energy Convers.,* vol. 27, no. 2, pp. 308-317, Jun. 2012.

[7] Z. Q. Zhu, M. M. J. Al-Ani, X. Liu, and B. Lee, "A mechanical flux weakening method for switched flux permanent magnet machines," *IEEE Trans. Energy Convers.*, vol. 30, no. 2, pp. 806-815, Jun. 2015.

[8] L. Del Ferraro, F. Caricchi, and F. G. Capponi, "Analysis and comparison of a speed-dependent and a torque-dependent mechanical device for wide constant power speed range in AFPM starter/alternators," *IEEE Trans. Power Electr.*, vol. 21, no. 3, pp. 720-729, May 2006.

[9] V. Ostovic, "Memory motors," *IEEE Ind. Appl. Mag*., vol. 9, no. 1, pp. 52-61, Jan./Feb. 2003.

[10] N. Limsuwan, T. Kato, K. Akatsu, and R. Lorenz, "Design and evaluation of a variable-flux flux-intensifying interior PM machine," *IEEE Trans. Ind. Appl*., vol. 50, no. 2, pp. 1015-1024, Mar./Apr. 2014.

[11] M. Ibrahim, L. Masisi, and P. Pillay, "Design of variable flux PM machine for reduced inverter rating," *IEEE Trans. Ind. Appl*. vol. 51, no. 5, pp. 3666-3674, Sep./Oct. 2014.

[12] K. Sakai, K. Hagiwara, and Y. Hirano, "High-power and high-efficiency permanent-magnet reluctance motor for hybrid electric vehicle," *TOSHIBA REVIEW Japan*, vol. 60, No.11, pp. 41-44, Sep. 2005.

[13] S. Maekawa, K. Yuki, M. Matsushita, I. Nitta, Y. Hasegawa, T. Shiga, T. Hosoito, K. Nagai, and H. Kubota, "Study of the magnetization method suitable for fractional-slot concentrated-winding variable magnetomotive-force memory motor," *IEEE Trans. Power Electron.*, vol. 29, no. 9, pp. 4877-4887, Sep. 2014.

[14] C. Yu and K. T. Chau, "Design, analysis, and control of DC-excited memory motors," *IEEE Trans. Energy Convers.*, vol. 26, no. 2, pp. 479-489, Jun. 2011.

[15] X. Zhu, L. Quan, D. Chen, M. Cheng, Z. Wang, and W. Li, "Design and analysis of a new flux memory doubly salient motor capable of online flux control," *IEEE Trans. Magn.*, vol. 47, no. 10, pp. 3220-3223, Oct. 2011.

[16] H. Yang, H. Lin, J. Dong, J. Yan, Y. Huang, and S. Fang, "Analysis of a novel switched-flux memory motor employing a time-divisional magnetization strategy," *IEEE Trans. Magn.*, vol. 50, no. 2, Art. No. 7021004, Feb. 2014.

[17] H. Yang, Z. Q. Zhu, H. Lin, S. Fang, and Y. Huang, "Comparative study of novel variable-flux memory machines having stator permanent magnet topologies" *IEEE Trans. Magn.*, vol. 51, no. 11, Art. no. 8114104, Nov. 2015.

[18] H. Yang, Z. Q. Zhu, H. Lin, S. Fang, and Y. Huang, "Synthesis of hybrid magnet memory machines having separate stators for traction applications," *IEEE Trans. Veh. Tech*., in press.

[19] H. Yang, Z. Q. Zhu, H. Lin, Y. Zhang, S. Fang, Y. Huang, and N. Feng, "Performance improvement of partitioned stator switched flux memory machines with triple-magnet configuration," *IEEE Trans. Magn.*, vol. 52, no. 7, Article. 8104604, Jul. 2016.

[20] D. Evans and Z. Q. Zhu, "Novel partitioned stator switched flux permanent magnet machines," *IEEE Trans. Magn*., vol. 51, no. 1, Art. no. 8100114, Jan. 2015.

[21] E. Hoang, A. H. Ben-Ahmed, and J. Lucidarme, "Switching flux PM polyphased synchronous machines," in *Proc. 7th Eur. Conf. Power Electron. Appl*., 1997, vol. 3, pp. 903–908.

[22] L. Jian, G. Xu, C. C. Mi, K. T. Chau, and C. C. Chan, "Analytical method for magnetic field calculation in a low-speed permanent-magnet harmonic machine," *IEEE Trans. Energy Convers*., vol. 26, no. 3, pp. 862-870, Sept. 2011.

[23] L. Wang, J. Shen, P. C.-K. Luk, W. Fei, C. Wang, and H. Hao, "Development of a magnetic-geared permanent-magnet brushless motor," *IEEE Trans. Magn.*, vol. 45, no. 10, pp. 4578–4581, Oct. 2009.

[24] Z. Z. Wu and Z. Q. Zhu, "Analysis of magnetic gearing effect in partitioned stator switched flux PM machines," *IEEE Trans. Energy Convers*., vol. 31, no. 4, pp. 1239-1249, Dec. 2016.

[25] G. Qi, J. T. Chen, Z. Q. Zhu, D. Howe, L. B. Zhou, and C. L. Gu, "Influence of skew and cross-coupling on flux-weakening performance of permanent magnet brushless AC machines," *IEEE Trans. Magn.*, vol. 45, no. 5, pp. 2110–2117, May 2009.

[26] W. Q. Chu, Z. Q. Zhu, J. Zhang, X. Liu, D. A. Stone, and M. P. Foster, "Investigation on operational envelopes and efficiency maps of electrically excited machines for electric vehicle applications," *IEEE Trans. Magn.*, vol. 51, no. 4, Art. no. 8103510, Apr. 2015.

[27] H. Hua, Z.Q. Zhu, C. Wang, M. Zheng, Z. Z. Wu, D. Wu, and X. Ge, "Partitioned stator machines with NdFeB and ferrite magnets," *IEEE Trans. Ind. Appl.*, vol.53, no.3, pp.1870-1882, 2016.